Aluminium-oxide wires for superconducting high kinetic inductance circuits

H Rotzinger[1], S T Skacel[1], M Pfirrmann[1], J N Voss[1], J Münzberg[1], S Probst[1], P Bushev[1], M P Weides[1], A V Ustinov[1,2] and J E Mooij[1,3]

[1] Physikalisches Institut, Karlsruher Institut für Technologie, Wolfgang-Gaede-Str. 1, D-76131 Karlsruhe, Germany
[2] Russian Quantum Center, National University of Science and Technology MISIS, Moscow 119049, Russia
[3] Kavli Institute of NanoScience, Delft University of Technology, Lorentz weg 1, 2628 CJ Delft, The Netherlands

E-mail: hannes.rotzinger@kit.edu

Abstract
We investigate thin films of conducting aluminium-oxide, also known as granular aluminium, as a material for superconducting high quality, high kinetic inductance circuits. The films are deposited by an optimised reactive DC magnetron sputter process and characterised using microwave measurement techniques at milli-Kelvin temperatures. We show that, by precise control of the reactive sputter conditions, a high room temperature sheet resistance and therefore high kinetic inductance at low temperatures can be obtained. For a coplanar waveguide resonator with $1.5\,k\Omega$ sheet resistance and a kinetic inductance fraction close to unity, we measure a quality factor in the order of 700 000 at 20 mK. Furthermore, we observe a sheet resistance reduction by gentle heat treatment in air. This behaviour is exploited to study the kinetic inductance change using the microwave response of a coplanar wave guide resonator. We find the correlation between the kinetic inductance and the sheet resistance to be in good agreement with theoretical expectations.

S Online supplementary data available from stacks.iop.org/sust/30/025002/mmedia

Keywords: superconductivity, kinetic inductance, thin film

(Some figures may appear in colour only in the online journal)

1. Introduction

Superconducting wires with a high kinetic inductance have been an active research topic in the past two decades in several different research areas [1]. From a technological perspective, the wires offer the possibility to overtop the geometric inductance by orders of magnitude and therefore allow, for instance, for very compact microwave resonator structures [2]. Also, the steep temperature dependence in the vicinity of the superconducting transition temperature can be used as a sensitive thermometer in superconducting low-frequency [3] and microwave particle detectors [4]. An emerging new field is the use of superconducting high kinetic inductance wires for parametric amplification of microwave signals

[5], e.g. for superconducting qubit measurements. In this field, a wire with a large kinetic inductance may replace also arrays of Josephson junctions, which are often used to enhance the inductance of a circuit. More fundamentally, a high kinetic inductance is among other aspects a mandatory ingredient for quantum phase slip measurements [6–10] and also in the context of experiments with quantum phase transitions [11, 12].

In this paper, we explore a new possibility of using aluminium oxide (AlO_x) for obtaining a high kinetic inductance in the superconducting state. The material has been researched as a *granular* superconductor, often referred to as *granular aluminium*, since the late 1960s [13–17] until now [18, 19], with a large body of publications on the film

1

properties, transport measurements and even absorptive microwave measurements [20–22]. However, the available high kinetic inductance of structured superconducting wires was not of interest.

Conventionally, the previously studied films have been prepared in a low pressure oxygen atmosphere and by thermal evaporation of pure aluminium. By employing this method, the room temperature electrical sheet resistance can be varied on a large scale from low ohmic (mΩ), over very high ohmic (kΩ) and to electrically insulating by simply adjusting the oxygen partial pressure. The obtained films cannot be considered microscopically 'homogenous' due to the intrinsic granularity. The grain size in the high ohmic regime was determined with transmission electron microscope imaging to about 4 nm[4].

The large range of possible sheet resistances stem from the variable thickness of a thin aluminium-oxide layer that is covering the individual aluminium grains. From this perspective the films can be seen as a network of Josephson junctions mediating the superconducting transport, with a very sensitive dependence on the insulating layer thickness and thus the implanted oxygen content [15].

In the following, we are purely interested in superconducting films at temperatures much below the transition temperature of about 1.6–1.8 K (20 nm thick films). To obtain a superconducting film, however, the normal state sheet resistance R_n should be roughly below the quantum resistance $R_q = h/4e^2 = 6.45$ kΩ [23, 24].

For functional wires with a large kinetic inductance also the film quality and R_n reproducibility in the sub R_q range are key aspects. Instead of the thermal evaporation technique, we have focused on controlling R_n by employing a reactive DC magnetron *sputtering process* in an oxygen atmosphere. This method is described in section 3. In section 3.2 we discuss the R_n dependence on thermal annealing at room temperature. The results are used to study the kinetic inductance of AlO$_x$ wires structured as microwave coplanar waveguide resonators at mK temperatures (section 4).

2. Theoretical background

Similarly to an argumentation found, e.g. in [25, 26], the kinetic inductance L_{kin} of a superconducting wire can be derived using the Bardeen–Cooper–Schrieffer (BCS) theory. In the low frequency limit ($hf \ll k_B T$), the Mattis–Bardeen formula for the complex conductivity in the local, dirty limit can be written in terms of the ratio of the imaginary conductivity σ_2 to the normal state conductivity σ_n

$$\frac{\sigma_2}{\sigma_n} = \frac{\pi\Delta(T)}{hf}\tanh\frac{\Delta(T)}{2k_B T},$$

where $\Delta(T)$ is the superconducting energy gap. Using the BCS relation $\Delta(0) = 1.76k_B T_c$, the expression simplifies at temperatures much below T_c to $\sigma_2/\sigma_n =$

$\pi\Delta(0)/hf = 1.76\pi k_B T_c/hf$. The imaginary component of the impedance is due to kinetic inductance $1/2\pi f\sigma_2$. At $T \ll T_c$ the total kinetic inductance $L_{kin,tot}$ of a wire with the length l and the width w can then be written as the product of the sheet inductance L_{kin} and the number of squares $N = l/w$

$$L_{kin,tot} = NL_{kin} = 0.18N\frac{\hbar R_n}{k_B T_c}, \tag{1}$$

where $R_n = 1/\sigma_n$ is the normal state sheet resistance. This handy formula is used at various places in this paper.

We use a coplanar waveguide (CPW) resonator made from AlO$_x$ at $T \ll T_c$ to obtain L_{kin} by measuring the resonance frequency. These data will be compared with L_{kin} evaluated from the sheet resistance. Neglecting the frequency shift induced by the coupling capacitors, the resonance frequency of a $\lambda/2$ CPW resonator is given by

$$f_n = (n + 1)/2l\sqrt{LC}, \tag{2}$$

where n is an integer harmonic number. The centre conductor inductance L and the capacitance of the centre conductor to ground C are per unit length. L constitutes of $L_m + g_{kin}L_{kin}$, the sum of the 'geometric' or 'magnetic' inductance L_m and the kinetic inductance L_{kin}. The factor $g_{kin} = \alpha N/l = \alpha/w$ is discussed in section 4.4, where α is in the order of unity. Using the conformal mapping technique, L_m and C are analytically found to be $L_m = \mu_0/4\ K(k')/K(k)$ and $C = 4\epsilon_0\,\epsilon_{eff}\,K(k)/K(k')$, where K is the complete elliptic integral of the first kind with the moments $k = w/(w + 2s)$ and $k' = \sqrt{(1 - k^2)}$ and s being the distance between the centre conductor and ground [27, 28], see also figure 4.

3. Sample fabrication and resistance measurements

The CPW resonators are fabricated in three steps, first, a 20 nm AlO$_x$ thin film is grown by DC magnetron sputter deposition on to an intrinsic or SiO$_2$ passivated 20×20 mm^2 Si substrate, details of this process are given below. The second step employs optical lithography to define the resonator structures on top of the AlO$_x$ thin film. Here we use the common 1 μm thick Clariant AZ-5214E optical resist and an UV-light mask aligner. The optical resist pattern is subsequently used as etch mask in a Cl/Ar 10:1 ICP/RIE plasma at 200 W/100 W etch process for 95 s. After that, the resist mask is removed and the substrate diced into 5×5 mm^2 chips.

3.1. Reactive DC sputter process

A common way of growing *ex situ* non-insulating AlO$_x$ thin films [13–15, 18] employs the thermal evaporation of aluminium in an oxygen atmosphere at about 1.0×10^{-5} mbar pressure. Initial experiments with a thermal e-beam evaporator and this technique showed an insufficient reproducibility of the sheet resistance at a given partial pressure of oxygen, especially for consecutive evaporations in the same chamber and with the same aluminium source. As a main reason for this, we identified the oxygen contamination of the

---

[4] The findings in [15] are in good agreement with the grain size measured on our sputter deposited films, see also online supplementary data.

hot, electron beam heated aluminium source. This limitation we overcome by using an Ar plasma DC and also a pulsed DC magnetron sputtering process. Here, the source is usually water cooled and it getters the injected oxygen ions only at the 'cleaned' surface. All films are deposited at room temperature.

We employ a home-made two-chamber sputter tool, having a base pressure of $<6 \times 10^{-8}$ mbar, with three $2''$ sputter targets, one equipped with 6 N purity Al. Prior to the sputter deposition, the samples are cleaned in the load lock using an RF Ar plasma for 2 min at a power of 20 W, mainly to remove water from the surface. Vital for reproducible results is the cleaning of the sputter target in the main chamber, which we do for at least 5 min in a pure Ar plasma at 100 W power. The reactive sputter process is then started by injecting 2.5 sccm Ar/O_2 9:1 mixture using a 10 sccm mass flow controller into the main chamber. The reactive plasma is stabilised at 100 W power and Ar flow of $\sim$40 sccm for approximately 1 min before a shutter is opened and the film is grown on a $\sim$60 rpm rotated sample for 3.5 min (rate ≈ 5.7 nm min^{-1}). We found the stability and resolution of the mass flow controllers as well as the pressure control to be important for reproducible results. The above parameters for the sputter process gave good results. Furthermore, we found several combinations of DC sputter powers and Ar/O_2 gas flow/pressure yielding similar results.

The target sheet resistance of AlO_x films depends on the amount of implanted oxygen in the film [13–15, 17] and, therefore, the ratio of the growth rate to the oxygen partial pressure. The sputter tool lacks a direct measurement of the growth rate e.g. through a quartz crystal monitor. Therefore, we use the Ar partial pressure as a control parameter and keep the oxygen flow constant. We are interested in the sheet resistance value range from 0.1 to 10 kΩ. In this range, the process parameters for R_n are well described by the following empirical formula $R_{sq} = R_0 + R \exp[(P - P_{off})/P_0]$ with P the Ar partial pressure. Least square fitting of data of various samples, see figure 1, yields to $R_0 = 0.5$ kΩ, $R = 0.11$ kΩ, $P_0 = 0.52 \times 10^{-3}$ mbar, keeping P_{off} fixed to 8×10^{-3} mbar. Not included here is a linear shift in the sputter conditions due to the target erosion, corrected over larger time scales. This shift was evaluated experimentally by using a test sample, prior to the deposition of the main samples. The effective thickness of the AlO_x films varies only by a few per cent, AFM measurements showed variations of less then 2 nm for a 20 nm film thickness.

It should be pointed out that using the described technique, in spite of the very sharp transition of AlO_x from a low ohmic to an insulating state, see figure 1, we were able to reach the targeted sheet resistance with an uncertainty of better than ±0.5 kΩ. This accuracy is sufficient for many applications employing highly resistive AlO_x.

3.2. Heat treatment of AlO_x films

If no lift off process is used, as for instance in [29], patterning of AlO_x films by post deposition etching and by using an optically or e-beam defined mask typically requires several
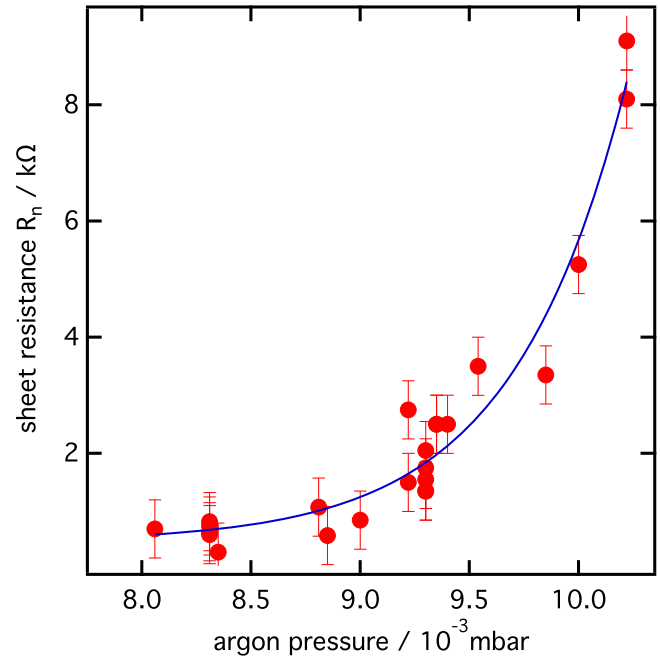

Figure 1. AlO_x sheet resistance depending on the Ar partial pressure during the sputtering process. The oxygen flow is kept constant for all films. The solid line is a fit to the data, details are given in the text.

steps with unavoidable heat treatments. Heat treatment by itself provides a convenient method of adjusting sample parameters after thin film processing. Therefore, we studied the dependence of R_n on thermal annealing for various AlO_x films grown on Si and SiO_2 substrates. Similarly to the lithography steps, we annealed the films on a preheated hotplate for several minutes in air and measured the film resistance after the samples have been cooled down to room temperature. The same sample is annealed for a time or temperature step, measured and annealed again. The set of samples measured for the time dependent annealing experiment is different to that of the temperature dependent measurement. Figure 2 shows the annealing time dependence of R_n for 20 nm thick AlO_x films annealed at a temperature of 250 °C. After a very steep decrease on the time scale of seconds, the sheet resistance R_n enters a plateau value at 400–500 s and changes only marginally for longer annealing times. A similar behaviour of the mechanical properties has been observed for bulk aluminium and aluminium-alloy samples, though on a timescale of hours [30].

Figure 3 shows the dependence of the normalised sheet resistance $R(T)/R(300 K)$ of annealed AlO_x films grown on Si and SiO_2 and over a wide range of initial sheet resistances. Shown is the average value of all measured samples at a given temperature and annealing time of 600 s. The inset of figure 3 contains the raw data as reference. When annealed below 200 °C, the sheet resistance of the AlO_x thin films changes only by about 10%, making this therefore fully compatible with conventional subsequent thin film patterning steps, i.e. the baking of lithographic resist. At 400 °C, the highest temperature that we have applied, we find a resistance reduction to about 22% of the initial value.
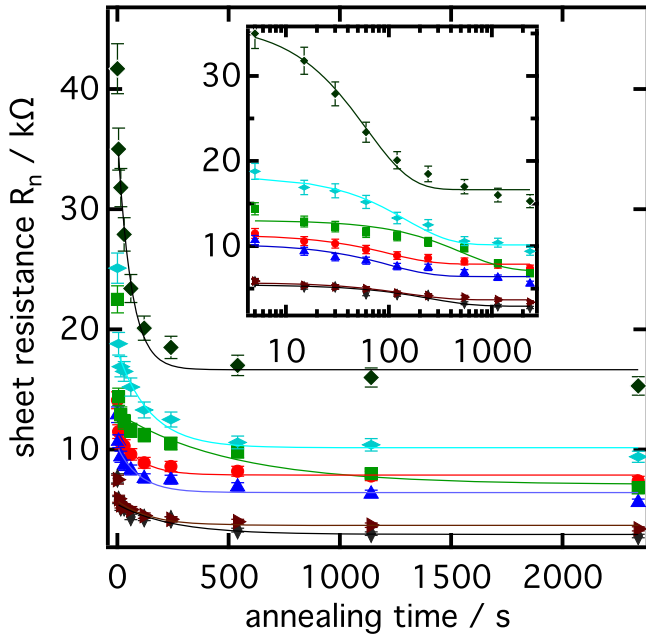
Figure 2. Time dependence of the AlO$_x$ sheet resistance at a fixed annealing temperature of 250 °C, overlaid are simple exponential decay curves as a guide to the eye. After ≈400–500 s the sheet resistance enters a plateau value and does only change very slowly with increased annealing time. The inset shows the same data on a logarithmic time scale.
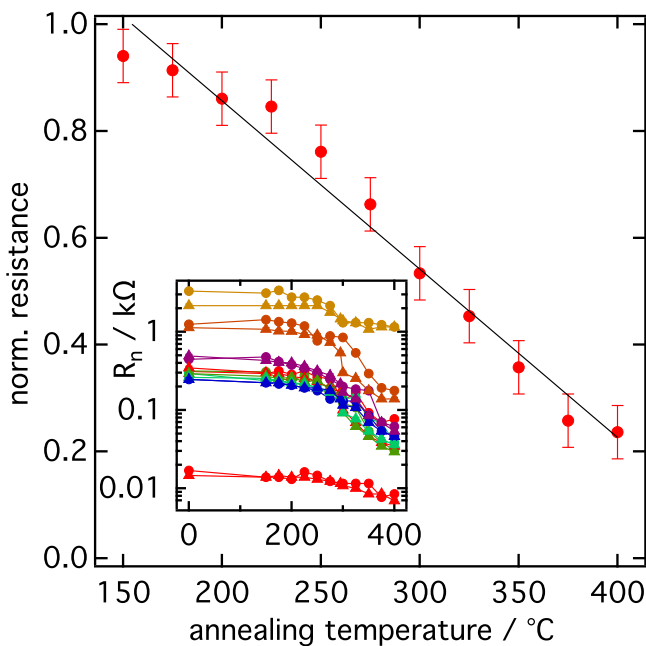

Figure 3. Normalised sheet resistance $R(T)/R(300\,\mathrm{K})$ of AlO$_x$ films versus the annealing temperature after an annealing time of 600 s. Shown is the average of films grown on Si and SiO$_2$ and having a wide range of initial sheet resistances. The inset contains the raw data of the measured films. The individual colours group samples which have been prepared in the same evaporation process, where triangles indicate a Si and circles a SiO$_2$ substrate.
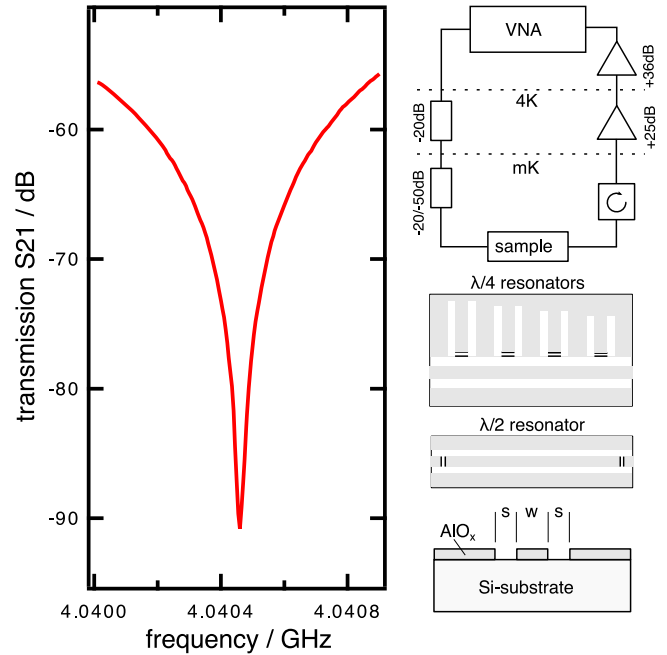

Figure 4. Microwave transmission measurement for a $\lambda/4$ resonator at −90 dB power level (left) and a sketch of the experimental setup including the CPW resonators (right).

Between 200 °C and 400 °C, the sheet resistance dependence with annealing temperature is found to be $R(T)/R(300\,\mathrm{K}) \approx$ 1.5–3.2 × 10^{-3} T/°C. This dependence is common to all samples, grown on Si or SiO$_2$ substrates, having R_n below $R_n \sim 20$ kΩ. Above this R_n value, a fraction of the samples showed an increase of the resistance by heat treatment.

The un-annealed samples do not show any signs of the intrinsic granularity of the AlO$_x$ films, measured by AFM scans (not shown). On the contrary, the rms surface roughness parameter $\tilde{R}_q$ for most of the un-annealed samples is well below 0.5 nm and is independent of the used substrates, SiO$_2$ or Si. In comparison, thermal or sputter grown pure aluminium films usually show $\tilde{R}_q$ values of around 1 nm or larger, due to the much larger grain size.

Concluding this section, we note a very low R_n drift <5%, in general towards higher R_n, at ambient storage temperatures measured over a period longer than one year.

4. Microwave measurements

4.1. Experimental setup

We have measured the transmission of $\lambda/2$ and feedline coupled $\lambda/4$ CPW resonators made of grown AlO$_x$ films using a ^{3}He cryostat at $T \approx 300$ mK and a cryogen free dilution refrigerator at $T \approx 20$ mK. The measurement scheme was very similar for both setups and is sketched in figure 4 (right). The microwave probe signal from a vector network analyser (VNA) was attenuated at different temperature stages by 40 dB (^{3}He) and by 70 dB (dilution refrigerator). In both

Table 1. Internal quality factor Q_i of a AlO_x $\lambda/4$ resonator measured at different power levels, at a resonance frequency $\omega_0 = 4.04$ GHz.

Power/dBm	−80	−90	−100	−115	−130
$Q_i/10^3$	343	668	674	329	126

setups, after passing the sample, the signal is amplified by 25 dB by a cryogenic HEMT amplifier. In the dilution refrigerator, an additional isolator at sample temperature reduces the back action of the amplifier onto the sample. At room temperature, a secondary amplifier boosts the signal by 36 dB before it is fed into the VNA. The sample is enclosed in a copper EM-tight microwave sample box, connecting it to semi-rigid microwave cables via a 50 Ω matched low-loss PCB.

4.2. Resonator samples

The samples were prepared by the deposition of a 20 nm thick AlO_x film having a sheet resistance $R_n = 0.5$ kΩ ($\lambda/2$ resonator) and $R_n = 1.5$ kΩ ($\lambda/4$ resonator) on an intrinsic Si substrate. The resist curing at 110 °C for 50 s and subsequent RIE etch did not change R_n significantly. We measured a residual resistivity ratio between room temperature and 4.2 K of 1.3 for both films.

4.3. Measurements at microwave frequencies

To measure the internal quality factor $Q_i = (Q^{-1} - Q_c^{-1})^{-1}$, we have designed and fabricated a set of $\lambda/4$ resonators with different couplings to a common feedline. Q is the total measured quality factor and Q_c the coupling quality factor due to the coupling capacitors. Figure 4 shows a typical resonance curve measured at 4.04 GHz frequency at −90 dB power level. For the designed $Q_c \approx 100\,000$, we measure internal quality factors ranging from 674 000 at intermediate to 126 000 at low (single photon) power levels, see table 1.

The measured Q_i values show that the disordered AlO_x films seem to have only very low internal dissipation. Without going into more detail, it is feasible that the losses are dominated by the usual dielectric losses seen in many recent CPW resonator measurements, e.g. as in [31, 32].

For determination of the kinetic inductance, we focus on the measurement of the $\lambda/2$ resonator. This resonator was measured twice, first without heat treatment, in a dilution refrigerator at 20 mK, and a second time after an annealing step at 250 °C for 10 min in the ^{3}He setup at about 300 mk[5]. Figure 5 shows an overlaid comparison of the two measurements, solid blue is the initial spectrum and the red crosses are the data after the heat treatment. Several harmonic frequencies of the resonator are clearly visible, the signal of the fundamental mode of both curves is suppressed by the lower cut-off frequency (∼2GHz) of the HEMT amplifiers. We find the base frequency by averaging the frequency spacing of the nth harmonic by $f_0 = f_n - f_{n-1}$, see table 2 for the obtained
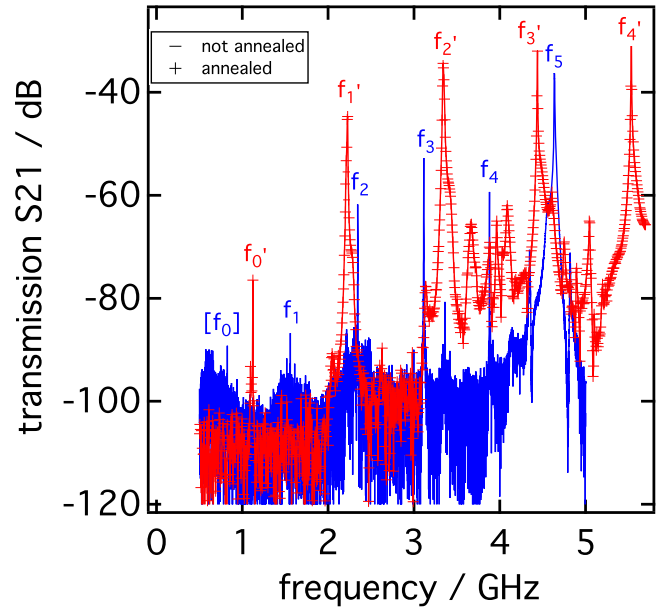
Figure 5. Comparison of the $\lambda/2$ CPW AlO_x resonator spectra measured before (blue dots) and after (red crosses) heat treatment at 250 °C for 10 min. Several harmonic resonances ($f_n = nf_0$ for the nth harmonic frequency) are visible in the measured frequency range. The fundamental mode f_0 of the un-annealed resonator (measured at $T = 20$ mK) is suppressed by the low frequency cut-off of the setup, but can be determined as $f_0 = f_n - f_{n-1}$. Due to the annealing, the sheet resistance and therefore the kinetic inductance both drop and f_0 is increased from 0.78 to 1.12 GHz by 340 MHz, see table 2 for details.

values. The internal quality factor of the over-coupled ($Q_l \approx 2000$) resonator at the third harmonic frequency evaluates to $Q_i \approx 37\,000$ at 20 mK. After annealing, the room temperature sheet resistance was lowered from 497 to 266 Ω.

4.4. Discussion

From a general point of view, the thin film resonator is a quasi two dimensional structure since its thickness $d = 20$ nm is of the order of the effective coherence length $\xi = \sqrt{\xi_0\,l}$. Following [15], ξ is of the order of the grain size ≈4 nm. An estimate of the penetration depth λ_L at $T \ll T_c$ is given by $1.05 \times 10^{-3}\sqrt{R_n\,d/T_c}$ m [27], for which we find $\lambda_L \approx 2.2\,\mu$m (un-annealed) and $\lambda_L \approx 1.6\,\mu$m (annealed). Therefore λ_L is much larger than the film thickness and also the perpendicular penetration depth $\lambda_{perp} = \lambda_L^2/d$ is much larger than the centre conductor width.

The AlO_x resonators were fabricated on intrinsic silicon ($\epsilon_r = 11.7$), therefore ϵ_{eff} is 6.3 [28]. With $w = 10\,\mu$m and $s = 6\,\mu$m, see figure 4, L_m and C are evaluated to be 438 nH m^{-1} and 160 pF m^{-1}, respectively. Using relation (2), we find a base resonance frequency of 6.7 GHz for the resonator with the length 8.96 mm, neglecting the kinetic inductance for a moment. This is reasonably close to a detailed high frequency EM finite element simulation data[6], which in addition includes also the geometrical details of the

---

[5] The relative frequency shift due to a change of the kinetic inductance between 20 and 300 mK is less than 10^{-3}, and can therefore be neglected.

[6] Sonnet Software, Inc., 2011, em Version 13.56, 100 Elwood Davis Road, North Syracuse, NY 13212, USA.
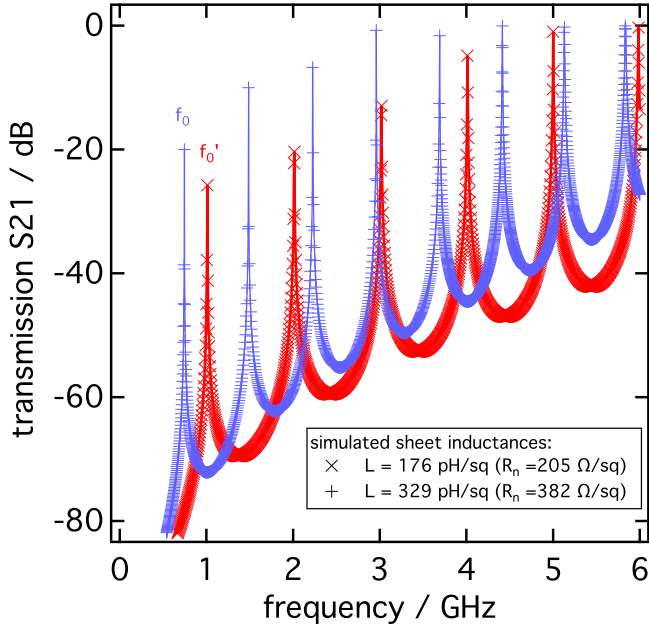
Figure 6. EM-simulation results of the $\lambda/2$-resonator with a sheet inductance 176 pH/sq (red, $\times$) and 329 ph/sq (blue, $+$). The sheet inductance was derived from the measured R_n value and equation (1). The simulated fundamental frequencies deviate from the measured frequencies by less than 10%, see also figure 5.

coupling capacitors. The EM solver calculates $f_0 = 6.9$ GHz as the base resonance frequency, thus the influence of the coupling capacitor contributes to about 3% in f_0 and is neglected in the further discussion.

If a kinetic sheet inductance derived from R_n and equation (1) is included in the EM-simulation, we obtain base frequencies of 745 MHz (un-annealed) and 1.01 GHz (annealed), see figure 6 for a spectrum from 0 to 6 GHz of the simulated S21 transmission. In the EM-simulation, the centre conductor and ground planes are treated as ideal conductors with the chosen material inductance to be the equivalent to the kinetic inductance corresponding to R_n, with no further 'superconducting' effects included. The calculation grid was set to 2 μm. Compared with the measured base frequencies the agreement is, likely due to the large λ_L, rather good, the EM-solver result overestimates the influence of the additional inductance by around 6% (un-annealed) and 10% (annealed).

In the analytic calculation, the high frequency pre-factor to the kinetic inductance $\alpha = g_{kin} w$ contains the details of the current distribution over the resonator cross section, which, in principle, also depends on the material's inductance. Instead of investigating the details of the current distribution in the centre conductor cross section or temperature

dependent measurements of λ_L, as treated e.g. in [33], we obtain α as a free parameter from the measured base frequency f_0 and R_n. With equation (1) and $\alpha = wL_{kin}^{-1}[((2f_0 l)^2 C)^{-1} - L_m]$, we find $\alpha = 0.96$ (un-annealed) and $\alpha = 0.86$ (annealed). Using the same method for comparison, we find from the EM-simulation data a constant value of $\alpha = 1.06$ for both R_n values.

It is interesting to note, that due to the large total inductance $L_{tot} = 1/(2f_0 l)^2 C = 286.4$ nH (un-annealed) and $L_{tot} = 138.7$ nH (annealed), we find a characteristic resonator impedance $Z_0 = \sqrt{L/C} = \sqrt{1/(2f_0 l)^2 C^2} = 447$ Ω (un-annealed) and $Z_0 = 311$ Ω (annealed). These high resonator impedance values may be an interesting property for microwave kinetic inductance detectors (MKID), because it can be easily matched e.g. to the vacuum impedance $Z_{0,vac} = \sqrt{\mu_0/\epsilon_0} = 377$ Ω [34]. Compared with the total magnetic inductance $L_{m,tot} = 3.9$ nH, we find a kinetic inductance fraction [35] $\alpha_{kin} = L_{kin,tot}/(L_{kin,tot} + L_{m,tot}) = 0.99$ and 0.97.

While it is possible to estimate the base frequency of a high kinetic inductance resonator by an EM-simulation, as we have shown above, we want to point out a less numerically intensive way of estimating a frequency shift by using equation (1).

The comparison of the values for the base frequency before (f_0) and after annealing (f_0'), can be written using relation (2) to $f_0/f_0' = ((L_m + g_{kin}' L_{kin}')/(L_m + g_{kin} L_{kin}))^{1/2}$. For resonators with a high kinetic inductance, $L_m \ll g_{kin} L_{kin}$, ($\alpha_{kin} \approx 1$), the relation approximates with equation (1) to

$$\frac{f_0}{f_0'} = \sqrt{\frac{L_{kin}'}{L_{kin}}} = \sqrt{\frac{T_c g_{kin}' R_n'}{T_c' g_{kin} R_n}}. \tag{3}$$

The T_c, f and R_n values are measured independently. In our case, $T_c = 1.6$ K was measured to be the same for both resonator measurements. For the g_{kin} change $g_{kin}' = k\, g_{kin}$ due to thermal annealing, we find with $k = (f_0/f_0')^2 R_n/R_n'$ a value of $k = 0.9$. We can therefore simplify equation (3) within an error margin of about 5% to $f_0/f_0' \approx \sqrt{R_n'/R_n}$. This result is of practical importance, because it allows to estimate a resonator base frequency by a simple sheet resistance measurement after thermal annealing.

5. Conclusion

In this paper, we show that by adding oxygen impurities to aluminium thin films, wires with a widely adjustable kinetic inductance at moderate film thicknesses can be obtained.

Table 2. AlO$_x$ $\lambda/2$ resonator properties.

Sample	R_n [a] Ω/sq	L_{kin} [b] pH/sq	T_c K	f_0 GHz	f_1 GHz	f_2 GHz	f_3 GHz	f_4 GHz	f_5 GHz
Un-annealed	382	329	1.6	[0.78]	1.56	2.34	3.11	3.87	4.65
Annealed	205	176	1.6	1.12	2.23	3.35	4.44	5.53	

[a] At 4.2 K, RRR = 1.3.
[b] See relation (1).

Fabricated with a controlled DC magnetron sputter growth process, we found robust conditions for room temperature sheet resistances in a range from 0.1 to several kΩ, corresponding to a high kinetic wire inductance in the superconducting state. As an option for lowering the sheet resistance, the AlO_x films can be annealed at moderate temperatures, R_n drops to about 1/5 of the initial value with a heat treatment at 400 °C.

Measurements of the microwave response of superconducting resonators confirm the high kinetic inductance. Moreover, the results demonstrate the potential of AlO_x to serve as a low-loss and high Q resonator material e.g. for MKID or compact resonators used, for instance, with superconducting qubit circuits.

Acknowledgments

References

[1] Rauch W, Gornik E, Sölkner G, Valenzuela A A, Fox F and Behner H 1993 Microwave properties of $YBa_2Cu_3O_{7-x}$ thin films studied with coplanar transmission line resonators *J. Appl. Phys.* **73** 1866–72

[2] Averkin A S, Zhuravel A P, Karpov A, Anlage S M and Ustinov A V 2013 Ultra-compact superconductive resonator with double-spiral structure *Advanced Electromagnetic Materials in Microwaves and Optics* pp 142–4

[3] Audley M D, Kelley R L and Rawley G L 1993 A prototype kinetic inductance thermometer for x-ray calorimetry *J. Low Temp. Phys.* **93** 245–50

[4] Day P K, LeDuc H G, Mazin B A, Vayonakis A and Zmuidzinas J 2003 A broadband superconducting detector suitable for use in large arrays *Nature* **425** 817–21

[5] Vissers M R, Hubmayr J, Sandberg M, Chaudhuri S, Bockstiegel C and Gao J 2015 Frequency-tunable superconducting resonators via nonlinear kinetic inductance *Appl. Phys. Lett.* **107** 062601

[6] Lau C N, Markovic N, Bockrath M, Bezryadin A and Tinkham M 2001 Quantum phase slips in superconducting nanowires *Phys. Rev. Lett.* **87** 217003

[7] Mooij J E and Nazarov Y V 2006 Superconducting nanowires as quantum phase-slip junctions *Nat. Phys.* **2** 169–72

[8] Arutyunov K Y, Golubev D S and Zaikin A D 2008 Superconductivity in one dimension *Phys. Rep.* **464** 1–70

[9] Astafiev O V, Ioffe L B, Kafanov S, Pashkin Y A, Arutyunov K Y, Shahar D, Cohen O and Tsai J S 2012 Coherent quantum phase slip *Nature* **484** 355–8

[10] Mooij J E, Schön G, Shnirman A, Fuse T, Harmans C J P M, Rotzinger H and Verbruggen A H 2015 Superconductor-insulator transition in nanowires and nanowire arrays *New J. Phys.* **17** 033006

[11] Schneider R, Zaitsev A G, Fuchs D and Löhneysen H V 2012 Superconductor-insulator quantum phase transition in disordered FeSe thin films *Phys. Rev. Lett.* **108** 257003

[12] Ovadia M, Kalok D, Sacepe B and Shahar D 2013 Duality symmetry and its breakdown in the vicinity of the superconductor-insulator transition *Nat. Phys.* **9** 415–8

[13] Abeles B, Cohen Roger W and Cullen G W 1966 Enhancement of superconductivity in metal films *Phys. Rev. Lett.* **17** 632–4

[14] Cohen R W and Abeles B 1968 Superconductivity in granular aluminum films *Phys. Rev.* **168** 444–50

[15] Deutscher G, Fenichel H, Gershenson M, Grünbaum E and Ovadyahu Z 1973 Transition to zero dimensionality in granular aluminum superconducting films *J. Low Temp. Phys.* **10** 231–43

[16] Abeles B 1976 Granular metal films *Applied Solid State Science* vol 6 (Amsterdam: Elsevier) pp 1–17

[17] Ziemann P, Heim G and Buckel W 1978 Oxygen content and oxide barrier thickness in granular aluminum films *Solid State Commun.* **27** 1131–5

[18] Bachar N, Lerer S, Hacohen-Gourgy S, Almog B and Deutscher G 2013 Kondo-like behavior near the metal-to-insulator transition of nanoscale granular aluminum *Phys. Rev.* B **87** 214512

[19] Bachar N, Pracht U S, Farber E, Dressel M, Deutscher G and Scheffler M 2014 Signatures of unconventional superconductivity in granular aluminum *J. Low Temp. Phys.* **179** 83–9

[20] D'Aiello R V and Freedman S J 1969 Microwave conductivity of granular superconducting aluminum films *J. Appl. Phys.* **40** 2156–60

[21] Stocker E and Buttet J 1985 Microwave study of granular superconducting Al films *Solid State Commun.* **53** 915–7

[22] Suss J T, Berlinger W, Portis A M, Mller K A, Jeanneret B and Martinoli P 1989 Anisotropic microwave absorption and dc resistance in magnetic fields of granular superconducting aluminum films *Solid State Commun.* **71** 929–33

[23] Haviland D B, Liu Y and Goldman A M 1989 Onset of superconductivity in the two-dimensional limit *Phys. Rev. Lett.* **62** 2180–3

[24] Jaeger H M, Haviland D B, Orr B G and Goldman A M 1989 Onset of superconductivity in ultrathin granular metal films *Phys. Rev.* B **40** 182–96

[25] Annunziata A J, Santavicca D F, Frunzio L, Catelani G, Rooks M J, Frydman A and Prober D E 2010 Tunable superconducting nanoinductors *Nanotechnology* **21** 445202

[26] Tinkham M 2004 *Introduction to Superconductivity* (*Dover Books on Physics* vol 1) 2nd edn (New York: Dover)

[27] Yoshida K, Watanabe K, Kisu T and Enpuku K 1995 Evaluation of magnetic penetration depth and surface resistance of superconducting thin films using coplanar waveguides *IEEE Trans. Appl. Supercond.* **5** 1979–82

[28] Simons R N 2001 *Coplanar Waveguide Circuits, Components, and Systems* (*Wiley Series in Microwave and Optical Engineering*) (Newark, NJ: Wiley)

[29] Wilson T E, Korolev K A and Crow N A 2015 Bilayer lift-off process for aluminum metallization *J. Micro/Nanolithography, MEMS, and MOEMS* **14** 014501

[30] Hatch J E 1984 *Aluminum: Properties and Physical Metallurgy* (Metals Park, OH: American Society for Metals)

[31] Gao J, Daal M, Vayonakis A, Kumar S, Zmuidzinas J, Sadoulet B, Mazin B A, Day P K and Leduc H G 2008 Experimental evidence for a surface distribution of two-level systems in superconducting lithographed microwave resonators *Appl. Phys. Lett.* **92** 152505

[32] Skacel S T, Kaiser Ch, Wuensch S, Rotzinger H, Lukashenko A, Jerger M, Weiss G, Siegel M and Ustinov A V 2015 Probing the density of states of two-level

tunneling systems in silicon oxide films using superconducting lumped element resonators *Appl. Phys. Lett.* **106** 022603

[33] Porch A, Lancaster M J and Humphreys R G 1995 The coplanar resonator technique for determining the surface impedance of $YBa_2Cu_3O_{7-\triangle}$ thin films *IEEE Trans. Microw. Theor. Tech.* **43** 306–14

[34] Monfardini A *et al* 2011 A dual-band millimeter-wave kinetic inductance camera for the IRAM 30 m telescope *Astrophys. J. Suppl. Ser.* **194** 24

[35] Gao J, Zmuidzinas J, Mazin B A, Day P K and Leduc H G 2006 Experimental study of the kinetic inductance fraction of superconducting coplanar waveguide *Nucl. Instrum. Methods Phys. Res.* A **559** 585–7

[36] Straumanis M E 1949 The precision determination of lattice constants by the powder and rotating crystal methods and applications *J. Appl. Phys.* **20** 726–34

[37] Dobrovinskaya E R, Lytvynov L A and Pishchik V 2009 Properties of Sapphire *Sapphire: Material, Manufacturing, Applications* (Boston, MA: Springer) pp 55–176